

## Evolution and lifetimes of flow topology in a turbulent boundary layer

G. E. Elsinga and I. Marusic

Citation: *Phys. Fluids* **22**, 015102 (2010); doi: 10.1063/1.3291070

View online: <http://dx.doi.org/10.1063/1.3291070>

View Table of Contents: <http://pof.aip.org/resource/1/PHFLE6/v22/i1>

Published by the [American Institute of Physics](#).

---

### Related Articles

Lagrangian evolution of the invariants of the velocity gradient tensor in a turbulent boundary layer  
*Phys. Fluids* **24**, 105104 (2012)

Effects of moderate Reynolds numbers on subsonic round jets with highly disturbed nozzle-exit boundary layers  
*Phys. Fluids* **24**, 105107 (2012)

Particle transport in a turbulent boundary layer: Non-local closures for particle dispersion tensors accounting for particle-wall interactions  
*Phys. Fluids* **24**, 103304 (2012)

Convection and reaction in a diffusive boundary layer in a porous medium: Nonlinear dynamics  
*Chaos* **22**, 037113 (2012)

Symmetry analysis and self-similar forms of fluid flow and heat-mass transfer in turbulent boundary layer flow of a nanofluid  
*Phys. Fluids* **24**, 092003 (2012)

---

### Additional information on *Phys. Fluids*

Journal Homepage: <http://pof.aip.org/>

Journal Information: [http://pof.aip.org/about/about\\_the\\_journal](http://pof.aip.org/about/about_the_journal)

Top downloads: [http://pof.aip.org/features/most\\_downloaded](http://pof.aip.org/features/most_downloaded)

Information for Authors: <http://pof.aip.org/authors>

### ADVERTISEMENT



**Running in Circles Looking  
for the Best Science Job?**

Search hundreds of exciting  
new jobs each month!

<http://careers.physicstoday.org/jobs>

physicstodayJOBS



# Evolution and lifetimes of flow topology in a turbulent boundary layer

G. E. Elsinga<sup>a)</sup> and I. Marusic<sup>b)</sup>

Department of Mechanical Engineering, The University of Melbourne, Victoria 3010, Australia

(Received 18 May 2009; accepted 24 November 2009; published online 11 January 2010)

The average rates of change in the invariants of the velocity gradient tensor ( $Q$  and  $R$ ) have been determined experimentally in the outer layer of a turbulent boundary layer as a function of the invariants themselves. Subsequent integration yields trajectories in the  $QR$  plane describing the average evolution of the local flow topology following a fluid particle. The trajectories reveal inward spiraling orbits around and converging to the origin. The orbit's period is nearly constant at  $14.3\delta/U_e$  corresponding to  $470\nu/u_\tau^2$ , which may be regarded as the characteristic lifetime of the energy containing eddies in this part of the boundary layer. Furthermore, an empirical model for the average  $Q$  and  $R$  evolution is presented that reproduces the main features of the orbits in the vicinity of the origin. The deviation of the  $QR$  trajectories of individual fluid particles from the average trajectory is discussed in relation to the significant scatter observed in the rates of change in the invariants around their average. © 2010 American Institute of Physics. [doi:10.1063/1.3291070]

## I. INTRODUCTION

Turbulence is not a purely random phenomenon, but instead is well known to contain topological flow structures that are coherent in time and space, commonly referred to as eddies or coherent structures.<sup>1</sup> They are fundamental to our present understanding of turbulence, and consequently, in relation to turbulent boundary layers (TBLs), the instantaneous spatial organization of eddies into hairpin vortices, packets, and very-large-scale motions has recently received important attention (see Adrian<sup>2</sup> for a review). However, open questions remain regarding the dynamics and time scales of these coherent motions.

In this study we provide a first step in that direction by describing experimental findings on the average evolution of the local flow topology in a TBL. In this evolution two time scales are observed related to changing topology by eddy interactions and to decaying topology by viscous diffusion, respectively. Average decay may suggest ultimate destruction of all the flow structures, but as will be shown later, new topology can develop from the converged end state.

For a nonrotating flow such as the zero-pressure-gradient TBL, the local topology at each point and at each time instant can be classified based on an evaluation of the velocity gradient tensor  $A_{ij} = \partial u_i / \partial x_j$ , as outlined by Chong *et al.*<sup>3</sup> In that study it was further shown that for an incompressible flow, the generalized topology depends solely on the second and the third invariants of this tensor,  $Q$  and  $R$ , which are given by

$$Q = -\frac{1}{2}A_{ij}A_{ji}, \quad (1)$$

$$R = -\frac{1}{3}A_{ij}A_{jk}A_{ki}.$$

The first invariant,  $P = -A_{ii}$ , is identically zero because of continuity. Hence the evolution of the flow topology in the

present boundary layer can be described by the development of  $Q$  and  $R$  in time.

The four main local topology classes are summarized in the  $QR$  phase plane in Fig. 1. Above the null discriminant line (i.e.,  $D = R^2/4 + Q^3/27 = 0$ ) the flow pattern is focal corresponding to a spiraling or vortical motion, while below this curve the pattern is of a combined node-saddle type (nonfocal), which has been associated mainly to strong dissipative structures.<sup>4</sup> Further subdivision can be made into so-called stable and unstable flow patterns based on the sign of  $R$ . Here an inward spiral or node is denoted stable ( $R < 0$ ), whereas an outward spiral or node is referred to as unstable ( $R > 0$ ). A complete discussion of these local topologies is given by Chong *et al.*<sup>3</sup> and Perry and Chong.<sup>5</sup>

In the past, investigations of the local flow topology in turbulence were almost exclusively dealing with direct numerical simulations (DNSs)<sup>6-8</sup> or analytical methods,<sup>9</sup> because they require all three components of velocity as well as their spatial derivatives to evaluate the invariants of velocity gradient tensors  $Q$  and  $R$ . Even with temporal information accessible, most of these studies are restricted to a description of the instantaneous flow. A procedure to investigate the average dynamic behavior of the invariants was proposed by Martín *et al.*<sup>10</sup> and Ooi *et al.*,<sup>11</sup> who studied the conditional average evolution of the local topology in DNS of isotropic turbulence and showed that these topology evolutions describe spiraling orbits in the  $QR$  space and tend to converge to a point (i.e., the origin).

Here this approach is extended to the larger scales of motion in the outer layer of a TBL ( $>50$  wall units) to establish characteristic lifetimes for the large, turbulent kinetic energy containing eddies. Through a comparison to DNS data some potentially universal aspects of the local flow topology dynamics across the range of scales and the different turbulent flows may be identified, as well as the differences. Furthermore, the development of new topology from the converged end state of the conditional average evolution will be addressed.

<sup>a)</sup>Present address: Laboratory for Aero and Hydrodynamics, Delft University of Technology. Electronic mail: g.e.elsinga@tudelft.nl

<sup>b)</sup>Electronic mail: imarusic@unimelb.edu.au.

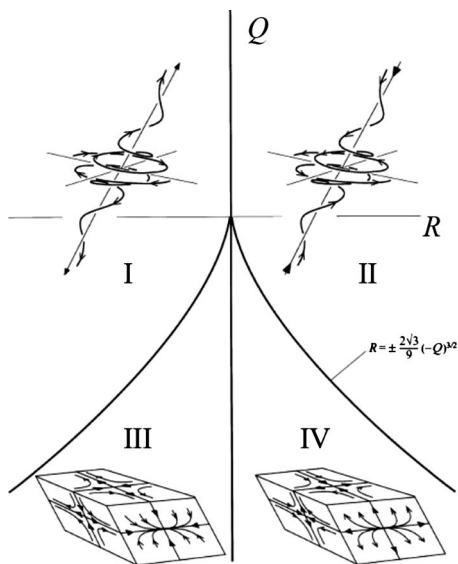


FIG. 1. Local flow topologies associated with the invariants of the velocity gradient tensors ( $Q$  and  $R$ ) for incompressible flow [taken from Ooi *et al.* (Ref. 11)]. I: stable focus/stretching, II: unstable focus/compressing, III: stable node/saddle/saddle, IV: unstable node/saddle/saddle.

One of the novel aspects of the present study is the experimental approach enabled by recent advances in velocimetry methods, in particular, tomographic particle image velocimetry (PIV).<sup>12,13</sup> It is an extension of standard planar PIV capable of instantaneously measuring all three components of velocity in a three-dimensional (3D) volume, which allows an assessment of the velocity gradient tensor. The method can be extended even further to 3D time-resolved measurements by using high repetition rate PIV hardware.<sup>14</sup>

In the remainder of the paper, the experimental data set is introduced (Sec. II) and the instantaneous joint probability density function (pdf) of the invariants of the velocity gradient tensor is discussed (Sec. III). Then the method to obtain the average dynamics of the invariants will be presented in Sec. IV with the results given. From the substitution of these results in the Navier–Stokes equations rewritten in terms of the velocity gradient tensor (Sec. V), the average effect of the eddy interactions can be inferred, which will also lead to the formulation of an empirical model for the dynamics of  $Q$  and  $R$  (Sec. VI). Some aspects regarding the data scatter and the creation of new topologies are discussed in Sec. VII, and Sec. VIII presents the conclusions.

## II. EXPERIMENTAL DATASET

The zero-pressure-gradient TBL data used in this investigation have been obtained from a time-resolved tomographic PIV experiment in the water tunnel of the Aero and Hydrodynamics Laboratories of TU Delft. The setup and first results of this collaborative effort between TU Delft Aerospace Engineering, TU Delft Laboratory for Aero and Hydrodynamics, and DLR Göttingen have been described in Refs. 15 and 16. For completeness, however, we will briefly recall some of the boundary layer properties here. The boundary layer develops over a 2.5 m long flat plate with an elliptical leading edge at a free-stream flow velocity  $U_e$  of

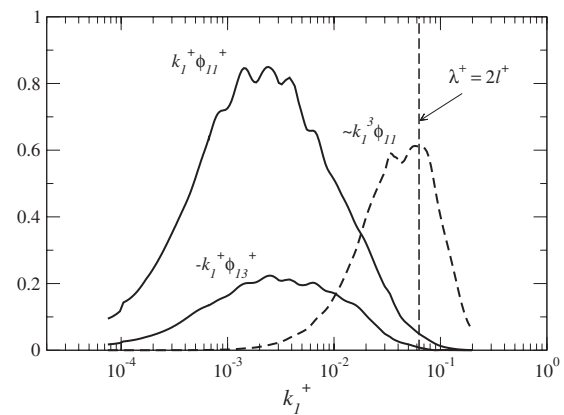


FIG. 2. Spectra and cospectra for  $z/\delta=0.16$  in a zero-pressure-gradient TBL at  $Re_\theta=2730$ , as reported by Nickels and Marusic (Ref. 18). To demonstrate that the energetic scales are captured, a vertical dashed line is added to show the maximum resolvable wave number corresponding to a wavelength of twice the size of the PIV interrogation window ( $l^+=50$ ), which is clearly beyond the energy-containing wave numbers that contribute significantly to the streamwise turbulence intensity or Reynolds shear stress.

0.53 m/s. Transition is imposed 15 cm downstream of the elliptical leading edge by a zigzag strip. At the measurement location, 2.0 m downstream, the boundary layer thickness  $\delta$  is 37 mm, and the Reynolds number based on momentum thickness and free-stream velocity,  $Re_\theta$ , and the friction Reynolds number,  $Re_\tau=U_\tau\delta/\nu$ , are 2460 and 800, respectively. Here  $U_\tau$  is the friction velocity and  $\nu$  is the kinematic viscosity.

The 3D velocity distribution  $V(x, y, z, t)$  is evaluated in a volume spanning  $1.8\delta \times 1.8\delta$  in streamwise  $x$  and spanwise  $y$  direction and covering  $z/\delta \in [0.11, 0.30]$  in the wall-normal ( $z$ ) direction over a period of 2 s. The sampling frequency is 1 kHz, corresponding to  $70U_e/\delta$  and  $\Delta t^+=0.47$ , indicating that it is well time resolved. Between subsequent measurement volumes in time, the flow structures advect by approximately ten wall units,  $\nu/u_\tau$ .

An important aspect of the measurements is the effect of spatial resolution. In these experiments the cross-correlation interrogation volume for the tomographic PIV is  $0.07\delta$  corresponding to approximately 50 wall units,  $\nu/u_\tau$ , in each direction. Across the near-wall region of the boundary layer, such a spatial resolution would pose a problem, but here we are concerned with the outer region of the flow ( $0.11 < z/\delta < 0.30$  corresponding to  $88 < z^+ < 240$  where  $z^+=u_\tau z/\nu$ ). Moreover, the focus of our study is on the large energy-containing eddies of the flow, which do not necessarily correspond to the majority of the vorticity associated with the inertial subrange and dissipation regions. To check that these motions are reliably resolved, comparisons were made using the DNS channel flow data of del Álamo *et al.*<sup>17</sup> at  $Re_\tau=934$ . The DNSs were spatially filtered in all directions equivalent to 50 wall units and were found to still account for over 98% of the Reynolds shear stress in the outer region. This comparison is reassuring, but limited since the outer region of a boundary layer and channel flow are not identical. For this reason, more detailed comparisons were made

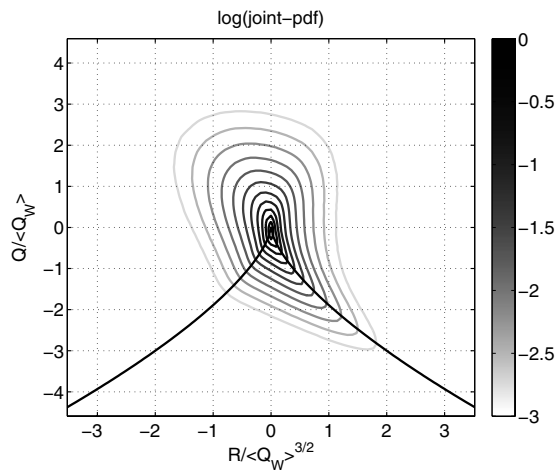


FIG. 3. Normalized joint pdf of  $Q$  and  $R$  on a logarithmic scale. The black solid line indicates points for which the discriminant of the velocity gradient tensor equals zero.

with our studies in TBL flows, at comparable Reynolds numbers, where fully resolved spectra and cospectra are available.

Figure 2 shows such a result for a hot-wire study in a TBL conducted in a wind tunnel at  $Re_\theta = 2730$ , as reported by Nickels and Marusic.<sup>18</sup> Premultiplied  $u$ -spectra and the cospectra are shown for a nominal position in the outer region, where in this semilogarithmic representation the area under the curves corresponds to streamwise turbulence intensity and Reynolds shear stress, respectively. Also shown in the figure is a dashed curve, which, based on isotropic flow assumptions, gives an indication of the contribution to the turbulent dissipation rate (the area under the dashed curve). A vertical line is also shown indicating the wave number above which spatial resolution effects may be regarded as significant. The results in Fig. 2 clearly show that while the smallest-scale motions, associated with dissipation and enstrophy, may not be fully resolved at this outer level of the boundary layer, the contributions from the energy-containing eddies that produce the turbulence intensity and the Reynolds shear stress are, essentially, fully resolved. Further comparisons to premultiplied velocity power spectra presented in Balakumar and Adrian<sup>19</sup> and Hutchins and Marusic<sup>20</sup> indicate a similar result.

### III. INSTANTANEOUS DISTRIBUTION OF THE INVARIANTS OF THE VELOCITY GRADIENT TENSOR

As a starting point for the discussion of the time evolution, we first consider the instantaneous distribution of the invariants. A statistical description of the volume and time average distribution of  $Q$  and  $R$  is given by their joint pdf in Fig. 3, where the invariants are normalized using  $\langle Q_W \rangle$ , the average of the second invariant of the rate of rotation tensor (following Ooi *et al.*<sup>11</sup>). The contour lines exhibit the self-similar “teardrop” shape around the origin that has also been observed in DNS studies of mixing layers, isotropic turbulence, channel, and boundary layer flow.<sup>7,11,21,8</sup> The similarity in these plots across the different flow cases has even

inspired some speculation about a kind of universality in the invariant space of turbulence.<sup>11</sup> Moreover, the favorable comparison between limited spatial resolution PIV and fully resolved DNS may further suggest that this extends beyond the smallest scales of motion. The potential of universality may therefore render a further statistical description of the evolution of turbulent structure in terms of  $Q$  and  $R$  very attractive.

### IV. DYNAMICS OF THE INVARIANTS

The dynamics of the invariants is investigated in a Lagrangian frame of reference moving with a fluid particle by means of their material derivatives, which are given by

$$\frac{DQ}{Dt} = \frac{\partial Q}{\partial t} + u \frac{\partial Q}{\partial x} + v \frac{\partial Q}{\partial y} + w \frac{\partial Q}{\partial z}, \quad (2)$$

$$\frac{DR}{Dt} = \frac{\partial R}{\partial t} + u \frac{\partial R}{\partial x} + v \frac{\partial R}{\partial y} + w \frac{\partial R}{\partial z}.$$

Note that all the terms on the right hand side depend only on the velocity  $V(x, y, z, t)$ , hence Eq. (2) can be evaluated directly for the present data set without further assumptions. Additionally, a conditional averaging technique is employed to obtain the mean temporal rate of change in the invariants  $Q$  and  $R$  as a function of invariants themselves. The averaging procedure is identical to the one of Ooi *et al.*<sup>11</sup> and reads as

$$\begin{aligned} \left\langle \frac{DQ}{Dt} \right\rangle (Q_0, R_0) &= \left\langle \frac{DQ}{Dt} \middle| -\frac{1}{2} \leq \frac{Q - Q_0}{\Delta Q} < \frac{1}{2}; -\frac{1}{2} \right. \\ &\quad \left. \leq \frac{R - R_0}{\Delta R} < \frac{1}{2} \right\rangle, \\ \left\langle \frac{DR}{Dt} \right\rangle (Q_0, R_0) &= \left\langle \frac{DR}{Dt} \middle| -\frac{1}{2} \leq \frac{Q - Q_0}{\Delta Q} < \frac{1}{2}; -\frac{1}{2} \right. \\ &\quad \left. \leq \frac{R - R_0}{\Delta R} < \frac{1}{2} \right\rangle, \end{aligned} \quad (3)$$

where  $Q_0$  and  $R_0$  are the bin centers and  $\Delta Q$  and  $\Delta R$  define the bin size over which the material derivative is averaged. Their respective values are  $0.18 \langle Q_W \rangle$  and  $0.088 \langle Q_W \rangle^{3/2}$ , which yield a large number of samples per bin ( $> 10^5$  in the region of interest) necessary to average out turbulent fluctuations<sup>11</sup> as well as random measurement noise related to the calculation of derivatives from experimental data. The result of the averaging procedure is presented in Fig. 4 as a vector field in the  $QR$  plane. As seen from the plot, the magnitude of the mean rate of change in  $Q$  and  $R$  (proportional to the vector length) increases with increasing distance from the origin. However, along the  $R > 0$  part of the null discriminant curve (black solid line) the vector magnitude remains relatively small. These results are consistent with the trends observed from DNS data of isotropic turbulence.<sup>10,11</sup>

The conditional average rate of change field can be integrated, which produces a  $QR$  trajectory, as shown on top of the vectors in Fig. 4. The trajectory orbits around the origin in clockwise direction and spirals inward. So, on average, the

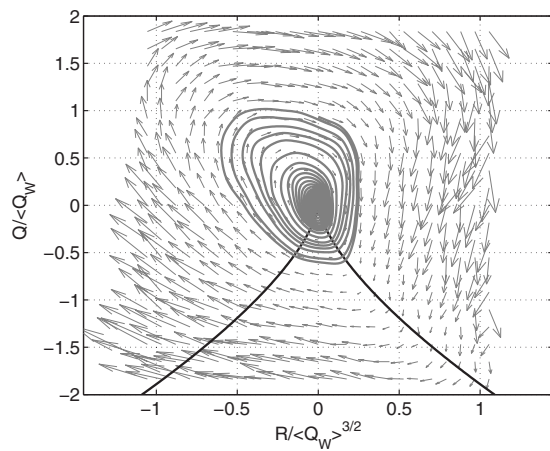


FIG. 4. Conditional averaged rate of change in  $Q$  and  $R$ , i.e., vectors of  $DQ/Dt$  and  $DR/Dt$ , and a corresponding  $QR$ -trajectory (spiraling solid line).

flow topology around a fluid particle changes cyclically from unstable focus, unstable node/saddle, stable node/saddle to stable focus (see Fig. 1). The values of  $Q$ ,  $R$ , and the discriminant  $D$  along the trajectory are plotted versus integration time in Fig. 5, each revealing a decrease with time corresponding to decreasing velocity gradients. Furthermore, the period of each orbit is found to be nearly constant at 1.00 s, corresponding to  $14.3\delta/U_e$  or  $10.4\langle Q_W \rangle^{-1/2}$  or  $470\nu/u_\tau^2$ , which may be regarded as a characteristic life-cycle time of the eddies in this region of the boundary layer ( $0.11 < z/\delta < 0.30$ ;  $88 < z^+ < 240$ , corresponding normally to the outer region, including part of the logarithmic region). The period is surprisingly close to the estimated eddy-turnover time for the large scale eddies  $\delta/u_{rms} = 14\delta/U_e$ , where the rms velocity is taken at the center of the measurement volume. Furthermore, the wavelength associated with the orbit's period is approximately  $11\delta$  (using the average velocity in the volume  $0.80U_e$  as the convective velocity). This corresponds reasonably well with the nominal location of where energy appears in the premultiplied power spectra of the streamwise component of velocity in wall-bounded turbulence corresponding to the very large-scale motions<sup>22,19</sup> or superstructures<sup>20</sup> observed in wall turbulence, which indi-

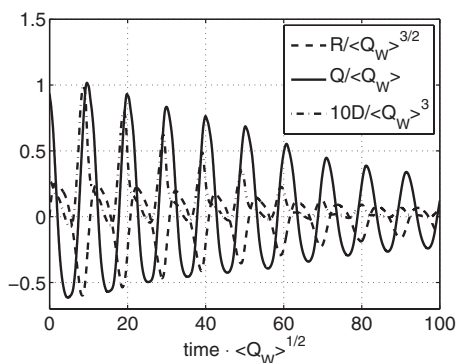


FIG. 5. Time evolution of  $Q$ ,  $R$ , and the discriminant  $D$  along the conditional average trajectory shown in Fig. 4.

TABLE I. Percentage of the time the  $QR$  trajectories spent in each of the topologies, as indicated in Fig. 1, for the large-scale motion in TBL and HIT [Martín *et al.* (Ref. 10)].

Topology	TBL (%)	HIT (%)
I: Stable focus	39	22
II: Unstable focus	38	20
III: Stable node	8	6
IV: Unstable node	15	53

cates that the eddies typically live over convective distances comparable to these very large scales.

The TBL flow is inhomogeneous in wall normal direction, and therefore the above time scales may potentially be affected by the applied averaging in the  $z$  direction. To check this, the measurement volume has been divided into three separate layers at different  $z$  repeating the described procedure for obtaining the invariants dynamics in each layer. No consistent trend with wall normal distance was found, which confirms the averaging does not introduce important errors. The variation in the orbit's period between the layers was about 10%, which is a measure for the accuracy of the present results.

Additionally, the results in Fig. 5 indicate that a second time scale may be defined that is representative of the invariants average decay rate over the cycles. The decay, resulting in the inward spiral, is associated with viscous diffusion, as shown by Martín *et al.*<sup>10</sup> (see their Fig. 14). Diffusion increases with increasing velocity gradients, hence magnitude of  $Q$  and  $R$ , which is consistent with the reduced decay rate near the origin and the orbits being more closely spaced there (Fig. 4). The estimated diffusion time scale is  $L^2/\nu = 300\delta/U_e = 9900\nu/u_\tau^2$ , where  $L = 0.13\delta = 104\nu/u_\tau$  is a representative length scale (taken as the smallest resolved wavelength). This shows diffusion acts on times an order of magnitude larger than the orbit's period, which is again consistent with the trajectory in Fig. 4. Based on the difference in magnitude we regard the orbit's period as the relevant topology lifetime dictated by the eddy interactions. (Note that ignoring the eddy interactions through both the pressure and viscous forces results in a completely different, nonperiodic evolution of the invariants.<sup>6,10,11</sup>)

The orbit's period here is different from the DNS of Martín *et al.*<sup>10</sup> for homogeneous isotropic turbulence (HIT), who report a period of three eddy-turnover times, equivalent to  $15\langle Q_W \rangle^{-1/2}$ . The discrepancy may be explained by the difference in the flows and flow scales investigated (small-scale isotropic in the case of Martín *et al.* and larger-scale anisotropic motions here). These differences become even more apparent when comparing the percentages of the orbit's period spent in each of the four topological states (Table I). For the large-scale motions in the present TBL, the average fluid particle spends relatively more time in a focal topology: 77% compared with 42% of the orbit in HIT. This time is split almost equally between the stable and unstable focus in both studies. Another profound difference is found for the unstable node part of the orbit: 15% (TBL) against 53% (HIT),

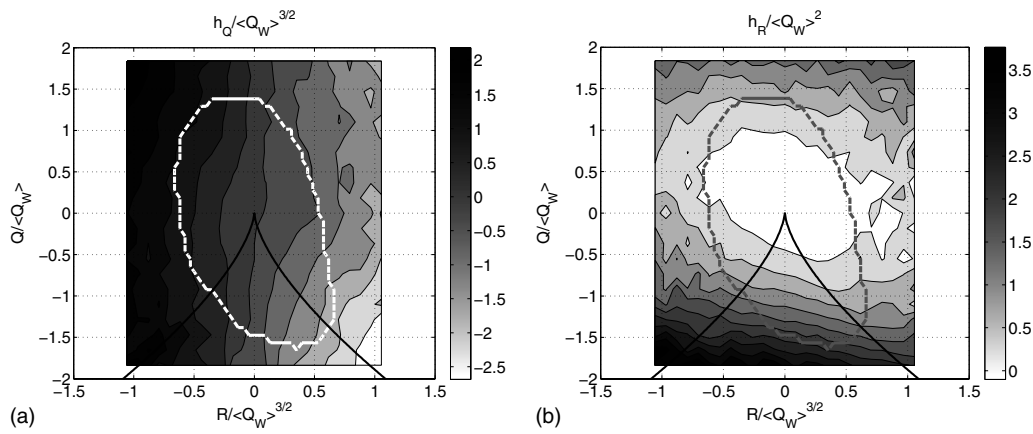


FIG. 6. Contour plots of the  $h_Q$  (left) and  $h_R$  (right) terms in Eq. (4), which relate to the contribution of the eddy interactions to the conditional averaged rate of change in  $Q$  and  $R$ , respectively. The dashed line indicates the region where the number of samples in each bin exceeds  $5 \times 10^5$ .

which must be related to the magnitude of the rates of change in the invariants being larger for the present large-scale motions. As a result the orbit's period decreases and the trajectory will not remain as long near the positive  $R$  branch of the null-discriminant curve. This part of the  $QR$  space has previously been associated to high rates of kinetic energy dissipation,<sup>6</sup> which is typically a small-scale phenomenon. This region is therefore likely to display differences. On the other hand, it was found that applying a low-pass filter to the present velocity data did not significantly alter the time scales obtained from the  $QR$  trajectories suggesting only a minor dependence of the result on the flow scale.

Martín *et al.*<sup>10</sup> further report that the trajectories are not perfectly self-similar especially the region corresponding to the nodal topologies, which is also observed here. This suggests a dependence on the distance of the trajectory from the origin. Hence, an additional explanation for the observed differences in the trajectories is given by the present trajectories being chosen closer to the origin.

## V. ANALYTICAL EXPRESSIONS

The obtained average rate of change can furthermore be inserted in the analytical expressions for the time evolution of the invariants, as derived from the Navier–Stokes equations in Cantwell.<sup>9</sup> Conditional averaging these expressions results in

$$\left\langle \frac{DQ}{Dt} \right\rangle (Q_0, R_0) = -3R_0 - \langle A_{ik} H_{ki} \rangle = -3R_0 - h_Q(Q_0, R_0),$$

$$\left\langle \frac{DR}{Dt} \right\rangle (Q_0, R_0) = \frac{2}{3} Q_0^2 - \langle A_{in} A_{nm} H_{mi} \rangle$$

$$= \frac{2}{3} Q_0^2 - h_R(Q_0, R_0),$$
(4)

with

$$H_{ij} = - \left( \frac{\partial^2 p}{\partial x_i \partial x_j} - \frac{\partial^2 p}{\partial x_k \partial x_k} \frac{\delta_{ij}}{3} \right) + \nu \frac{\partial^2 A_{ij}}{\partial x_k \partial x_k},$$
(5)

where  $\delta_{ij}$  is the Kronecker delta. The right hand side of Eq. (4) is composed of a contribution from local topology

through  $Q$  and  $R$  and a nonlocal contribution through the tensor  $H_{ij}$ , accounting for the interaction of adjacent fluid particles through pressure and viscous forces, which depends on the position of other eddies relative to the considered point in the flow. Hence the latter term will not be a unique function of local flow quantities such as  $Q$  and  $R$ . Consequently the adopted conditional averaging procedure yields the average effect of these eddy interactions.

To see the contribution of the eddy interactions, the  $h_Q$  and  $h_R$  terms in Eq. (4) are computed and presented in normalized form in Fig. 6. Again the results reveal a good qualitative agreement with those obtained by DNS of isotropic turbulence,<sup>10</sup> although only a more detailed view of the region near the origin is presented here. Furthermore, there appears to be a greater asymmetry in  $h_R$  in the  $Q$  direction in the present data consistent with the shorter time period the  $QR$  trajectories spend in the unstable node region, as mentioned above. From Fig. 6, it can also be seen that the  $h_Q$  and  $h_R$  terms are significant and are of the same order as the other right-hand-side terms in the invariant evolution equations, i.e., compare  $-3R$  and  $2/3Q^2$  along the coordinate axis with the contour levels. The sign of  $-h_Q$  is predominantly opposite to  $-3R$ , hence it has the effect of reducing  $DQ/Dt$  with respect to the inviscid, restricted Eulerian case ( $H_{ij}=0$ ).<sup>9</sup> Similarly,  $-h_R$  has the effect of reducing  $DR/Dt$ , so the pressure and viscous forces act to reduce the average rate of change in the invariants. Furthermore, the magnitude of  $h_R$  is larger than  $2/3Q^2$  for negative  $Q$  causing  $DR/Dt$  to become negative in that region, which consequently results in the observed spiraling  $QR$  trajectories. Hence, unstable nodes on average develop into stable nodes. Additionally, the pressure and viscous forces allow focal topologies to develop into nodal topologies and vice versa, as opposed to the restricted Eulerian case where focal and nodal topologies remain so indefinitely.<sup>9</sup>

## VI. AN EMPIRICAL MODEL

In the past, a number of theoretical models for the dynamic evolution of the invariants or the complete velocity gradient tensor in isotropic turbulence have been proposed and compared with DNS data in a qualitative way.<sup>10,23</sup> Chev-

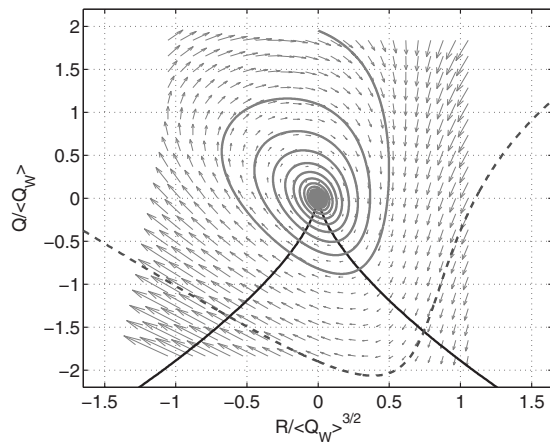


FIG. 7. Empirical model for  $DQ/Dt$  and  $DR/Dt$  (vectors) and resulting  $QR$ -trajectories (spiraling solid line and dashed separatrix).

illard *et al.*<sup>23</sup> were able to reproduce the spiraling  $QR$  trajectories very close to the origin in the  $QR$  plane, as in Fig. 4. However, for larger velocity gradients, especially in the region  $R < 0$ , there remains a clear difference with respect to the DNS results. This indicates that a further mathematical description of the invariant dynamics is still of some interest.

Therefore, the present results are synthesized by fitting relatively simple functions to  $h_Q$  and  $h_R$ , thereby producing an empirical model for these terms. Note that only data enclosed by the dashed line in Fig. 6 will be used, as the bins outside this region contain insufficient samples for convergence. Based on the contours in Fig. 6 a first order polynomial in  $Q$  and  $R$  is selected to approximate  $h_Q$ , while a second order polynomial is used for  $h_R$ . The polynomial coefficients are obtained from a least-squares regression resulting in the following simple model:

$$\frac{h_R}{\langle Q_w \rangle^{3/2}} = a_1 R^* + a_2 Q^* + a_3 R^* Q^* + a_4 R^{*2} + a_5 Q^{*2}, \quad (6)$$

$$\frac{h_Q}{\langle Q_w \rangle^2} = b_1 R^* + b_2 Q^*,$$

with

$$Q^* = \frac{Q}{\langle Q_w \rangle}; \quad R^* = \frac{R}{\langle Q_w \rangle^{3/2}}, \quad (7)$$

and where

$$\begin{aligned} a_1 &= -0.165; & a_2 &= -0.318, \\ a_3 &= 0.428; & a_4 &= 0.475; & a_5 &= 0.663, \\ b_1 &= -1.859; & b_2 &= 0.213. \end{aligned} \quad (8)$$

Inserting these functions in Eq. (3) returns a set of differential equations for a dynamical system of two variables, which can then be solved. The mean rate of change in  $Q$  and  $R$  is presented in Fig. 7 with trajectories. The dashed trajectory is a separatrix, above which the trajectories spiral inward as before. However, below this line, the trajectories go to infinity, which is believed to be unphysical. Hence the model can

be applied with confidence only inside the fitted region (marked by the dashed line in Fig. 6). Moreover, important differences between the model and the actual  $h_Q$  and  $h_R$  have been observed near the null discriminant curve and for large positive  $R$ , strongly suggesting additional terms will be required for improved accuracy and extrapolation later on. Determining the nature of these additional terms would require either theory or converged data over a larger area in the  $QR$  space, but preferably both.

Nevertheless, near the origin, the trajectories (the solid line in Fig. 7) reproduce the basic features of the measurement, such as the clockwise spiraling orbit, the decreasing value of the invariants with time, and the convergence to the origin. Even the orbit's period, 1.1 s corresponding to  $16\delta/U_e$ ,  $526\nu/u_\tau^2$ , and  $11\langle Q_w \rangle^{-1/2}$ , is in reasonable agreement (within 10%), so that the model may be regarded as a starting point for future refinements.

## VII. SOME REMARKS ON THE CREATION OF FLOW TOPOLOGY AND DATA SCATTER

The average results of Figs. 4 and 5 indicate a decay of  $Q$  and  $R$  with time, suggesting all flow topology is ultimately destroyed, i.e.,  $Q=R=0$  after some time. This may seem to go against the principle of statistically steady turbulence in the boundary layer, and raises questions as to how the creation of new topology is reflected in the  $QR$  plane. Here we consider some of these issues.

First of all, it must be noted that the origin does not only represent uniform flow (say free of any structured topology), but also shear layers, or vorticity sheets, which manifest themselves around the zero discriminant line in the  $QR$  space going through the origin. They represent a degenerate flow topology<sup>5</sup> with  $Q=R=0$  [Eq. (1)], which is readily seen from the case where  $A_{12} = \partial u / \partial y$  is the only nonzero entry in the velocity gradient tensor. Shear layers are well known to develop flow structures, most notably vortex structures. Evidence in support of this is given by the joint pdf of the invariants rate of change in the bin located at the origin [Fig. 8(a)], which shows a relatively large scatter in all directions. [Please note that the qualitative discussion of the scatter represents the turbulent fluctuations. This has been verified by filtering out the small-scale fluctuations in the invariants (predominantly measurement noise), which produced very similar results, at least qualitatively.] It indicates that all possible  $QR$  topologies can develop from the basic state  $Q=R=0$ , but on average they cancel resulting in the zero rate of change in the invariants. The creation of topology in the  $QR$  space may therefore be viewed as a random phenomenon obscured in the trajectories of Fig. 4 by the averaging process. It may further be conjectured that as a center focal structure ( $Q > 0$ ,  $R = 0$ , vortex) develops in a shear layer a nodal topology must develop at the same time, which is consistent with instantaneous topological constraints in a plane<sup>24</sup> and observations of spiral-saddle combinations in a rolling-up shear layer.<sup>5</sup>

The large scatter in the rate of change in the invariants is also found for other points in the  $QR$  plane [Figs. 8(b)–8(d)], which are consistent with the large number of samples re-

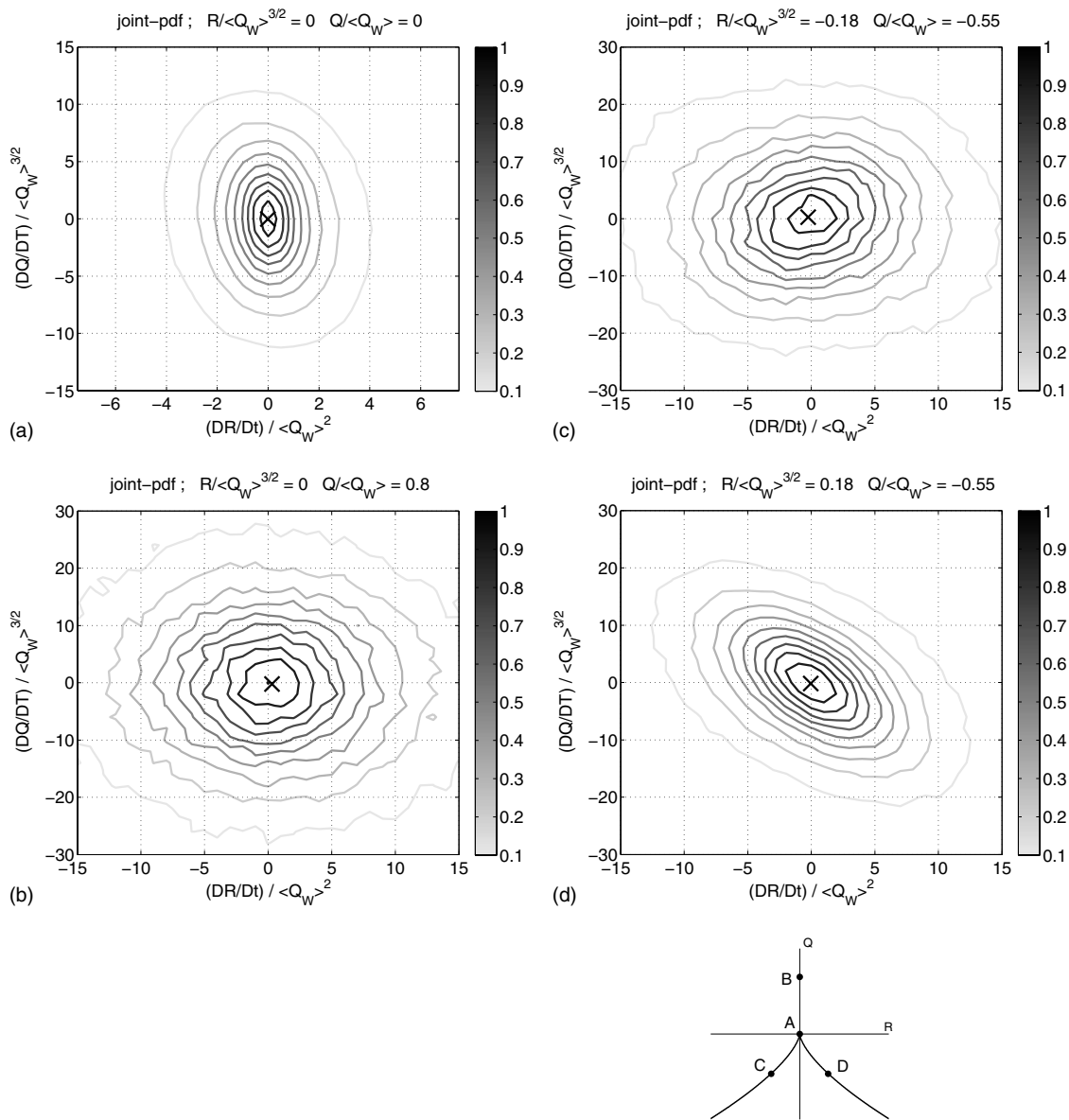


FIG. 8. Normalized joint pdf's of the invariants rate of change for four points in the  $QR$  space. (a) represents the origin, (b) a point on the positive  $Q$ -axis, (c) and (d) a point on the left and right branches of the null-discriminant curve, respectively. The average rate of change is indicated with  $X$ .

quired for convergence.<sup>10,11</sup> The scatter increases with distance from the origin and is clearly much larger than the average rate of change, which is indicated by an  $X$  in each plot. While most joint pdf's have a more or less circular shape [e.g., Figs. 8(b) and 8(c)], near the  $R > 0$  branch of the null-discriminant curve, the contours of equal probability are elongated in the direction of this curve, as seen in Fig. 8(d). This means the topology is more likely to change in the direction parallel to the null-discriminant curve rather than normal to it, which suggests a resistance of the flow to a change from unstable focus to unstable node and vice versa. The result is a low magnitude of the average rate of change in the invariants locally, as mentioned above. A similar but weaker elongation can be seen in the joint pdf for  $Q=R=0$  [Fig. 8(a)] in the direction which is slightly inclined from the  $Q$ -axis.

The significant scatter in the invariants rate of change will cause  $Q$  and  $R$  along individual particle paths to be very

different from the average trajectory presented in Fig. 4. That is, starting from the same initial condition  $(Q_0, R_0)$ , the individual  $QR$  paths will strongly diffuse from the average trajectory, and it is speculated that after a long time the joint pdf of  $Q$  and  $R$  for all these paths converges to the result of Fig. 3 for the instantaneous flow field.

## VIII. CONCLUSIONS

The evolution of the invariants of the velocity gradient tensors  $Q$  and  $R$  in the outer layer of a TBL has been studied using a conditional averaging approach. The invariants have been determined from time-resolved 3D experimental (tomographic PIV) velocity data and are representative of the local flow topology related to the larger, energy-containing scales of motion.

Both the instantaneous joint pdf of the invariants and their average temporal behavior are consistent with previous

DNS studies of small-scale motion in isotropic turbulence,<sup>10,11</sup> at least qualitatively. In the  $QR$  phase plane, the temporal evolution is characterized by an inward clockwise spiraling trajectory converging to the origin, which translates to the topology around a fluid particle varying cyclically from unstable focus, unstable node, stable node to stable focus, on average. The period of the spiral orbit is nearly constant and determined to be  $14.3\delta/U_e$ ,  $470\nu/u_\tau^2$  or  $10.4\langle Q_W \rangle^{-1/2}$  in the present flow, which may be regarded as a characteristic lifetime for the energy containing eddies in this outer region of the boundary layer ( $0.11 < z/\delta < 0.30$  corresponding to  $88 < z^+ < 240$ ). The spatial wavelength associated with this period is approximately  $11\delta$ , suggesting a relation with the very large scale motions in the boundary layer as observed in individual velocity fields and in the velocity power spectra.<sup>19,20</sup> Furthermore, some quantitative differences in the orbit's period with respect to the DNS of isotropic turbulence have been observed and discussed.

Inserting the present results into the invariant evolution equations yielded the average effect of the eddy interactions through the pressure and viscous forces. An attempt has been made to model these terms,  $h_Q$  and  $h_R$ , by curve fitting in order to create a simple set of dynamical system equations describing the average evolution of  $Q$  and  $R$ . This empirical model has been shown to reproduce the main features of the orbits in the  $QR$  plane. However, to capture all the details and improve the accuracy, more complex terms will need to be included in the model in future refinements.

A significant scatter is found around the average rate of change in the invariants, which means that for the same initial condition the  $QR$  paths of individual fluid particles will strongly diffuse from the average trajectory. The scatter also reflects the creation of new topology in the  $QR$  plane from the converged end state of the average trajectory (i.e., from the origin).

## ACKNOWLEDGMENTS

The authors wish to thank F. Scarano, C. Poelma, and J. Westerweel from T.U. Delft and A. Schröder and R. Geisler from DLR, Germany for providing the experimental data set. The Australian Research Council is gratefully acknowledged for their financial support.

<sup>1</sup>B. J. Cantwell, "Organized motion in turbulent flow," *Annu. Rev. Fluid Mech.* **13**, 457 (1981).

<sup>2</sup>R. J. Adrian, "Hairpin vortex organization in wall turbulence," *Phys. Fluids* **19**, 041301 (2007).

<sup>3</sup>M. S. Chong, A. E. Perry, and B. J. Cantwell, "A general classification of three-dimensional flow fields," *Phys. Fluids A* **2**, 765 (1990).

<sup>4</sup>J. M. Chacin and B. J. Cantwell, "Dynamics of a low Reynolds number turbulent boundary layer," *J. Fluid Mech.* **404**, 87 (2000).

<sup>5</sup>A. E. Perry and M. S. Chong, "A description of eddy motions and flow

patterns using critical-point concepts," *Annu. Rev. Fluid Mech.* **19**, 125 (1987).

<sup>6</sup>B. J. Cantwell, "On the behavior of velocity gradient invariants in direct numerical simulation," *Phys. Fluids A* **5**, 2008 (1993).

<sup>7</sup>J. Soria, R. Sondergaard, B. J. Cantwell, M. S. Chong, and A. E. Perry, "A study of the fine-scale motions of incompressible time-developing mixing layers," *Phys. Fluids* **6**, 871 (1994).

<sup>8</sup>M. S. Chong, J. Soria, A. E. Perry, J. Chacin, B. J. Cantwell, and Y. Na, "A study of the turbulence structures of wall-bounded shear flows using DNS data," *J. Fluid Mech.* **357**, 225 (1998).

<sup>9</sup>B. J. Cantwell, "Exact solution of a restricted Euler equation for the velocity gradient tensor," *Phys. Fluids A* **4**, 782 (1992).

<sup>10</sup>J. Martín, A. Ooi, M. S. Chong, and J. Soria, "Dynamics of the velocity gradient tensor invariants in isotropic turbulence," *Phys. Fluids* **10**, 2336 (1998).

<sup>11</sup>A. Ooi, J. Martín, J. Soria, and M. S. Chong, "A study of the evolution and characteristics of the invariants of the velocity-gradient tensor in isotropic turbulence," *J. Fluid Mech.* **381**, 141 (1999).

<sup>12</sup>G. E. Elsinga, F. Scarano, B. Wieneke, and B. W. Van Oudheusden, "Tomographic particle image velocimetry," *Exp. Fluids* **41**, 933 (2006).

<sup>13</sup>G. E. Elsinga, "Tomographic particle image velocimetry and its application to turbulent boundary layers," Ph.D. thesis, Delft University of Technology, 2008.

<sup>14</sup>A. Schröder, R. Geisler, G. E. Elsinga, F. Scarano, and U. Dierksheide, "Investigation of a turbulent spot and a tripped turbulent boundary flow using time-resolved tomographic PIV," *Exp. Fluids* **44**, 305 (2008).

<sup>15</sup>R. Geisler, A. Schröder, K. Staack, J. Kompenhans, G. E. Elsinga, F. Scarano, C. Poelma, J. Westerweel, B. Wieneke, and D. Michaelis, "Tomographic PIV for investigation of unsteady flows with high spatial and temporal resolution," in *Imaging Measurement Methods for Flow Analysis*, Notes on Numerical Fluid Mechanics and Multidisciplinary Design Vol. 106, edited by W. Nitsche and C. Dobriloff (Springer-Verlag, Berlin, 2009), pp.73–82; appeared also as A. Schröder, R. Geisler, K. Staack, B. Wieneke, G. E. Elsinga, F. Scarano, and A. Henning, "Lagrangian and Eulerian views into a turbulent boundary layer flow using time-resolved tomographic PIV," 14th International Symposium on Applications of Laser Techniques to Fluid Mechanics, Lisbon, Portugal, 2008.

<sup>16</sup>G. E. Elsinga, F. Scarano, A. Schröder, R. Geisler, C. Poelma, and J. Westerweel, "Experimental investigation of coherent structure dynamics in the outer layer of a turbulent boundary layer," XXII ICTAM, Adelaide, Australia, 2008.

<sup>17</sup>J. C. del Álamo, J. Jimenez, P. Zandonade, and R. D. Moser, "Scaling of energy spectra of turbulent channels," *J. Fluid Mech.* **500**, 135 (2004).

<sup>18</sup>T. B. Nickels and I. Marusic, "On the different contributions of coherent structures to the spectra of a turbulent round jet and a turbulent boundary layer," *J. Fluid Mech.* **448**, 367 (2001).

<sup>19</sup>B. J. Balakumar and R. J. Adrian, "Large- and very large-scale motions in channel and boundary-layer flows," *Philos. Trans. R. Soc. London, Ser. A* **365**, 665 (2007).

<sup>20</sup>N. Hutchins and I. Marusic, "Evidence of very long meandering features in the logarithmic region of turbulent boundary layers," *J. Fluid Mech.* **579**, 1 (2007).

<sup>21</sup>H. M. Blackburn, N. N. Mansour, and B. J. Cantwell, "Topology of fine-scale motions in turbulent channel flow," *J. Fluid Mech.* **310**, 269 (1996).

<sup>22</sup>K. C. Kim and R. J. Adrian, "Very large-scale motion in the outer layer," *Phys. Fluids* **11**, 417 (1999).

<sup>23</sup>L. Chevillard, C. Meneveau, L. Biferale, and F. Toschi, "Modeling the pressure Hessian and viscous Laplacian in turbulence: Comparisons with direct numerical simulation and implications on velocity gradient dynamics," *Phys. Fluids* **20**, 101504 (2008).

<sup>24</sup>J. F. Foss, "Surface selection and topological constraint evaluations for flow field analysis," *Exp. Fluids* **37**, 883 (2004).